



Cite this: DOI: 10.1039/c8dt04374d

Flexible $\text{Ti}_3\text{C}_2\text{T}_x$ /PEDOT:PSS films with outstanding volumetric capacitance for asymmetric supercapacitors†

Lu Li,^{a,b} Na Zhang,^c Mingyi Zhang,^b Xitian Zhang ^{*b} and Zhiguo Zhang ^{*a}

MXenes are two-dimensional transition metal carbides/nitrides, and they have shown exciting application prospects for electrochemical energy storage in the future owing to their hydrophilicity, metallic conductivity and surface redox reactions, which are crucial for high-capacitance and high-rate electrode materials. However, the strong tendency of adjacent MXene flakes to aggregate or self-restack under the van der Waals force limits the electrochemical performance of MXene-based electrodes for practical applications. In this study, we developed a simple and effective method to prepare $\text{Ti}_3\text{C}_2\text{T}_x$ /PEDOT:PSS hybrid films *via* filtering the $\text{Ti}_3\text{C}_2\text{T}_x$ /Clevios PH1000 compound inks, followed by H_2SO_4 treatment. H_2SO_4 treatment could remove part of the insulating PSS from the $\text{Ti}_3\text{C}_2\text{T}_x$ /PEDOT:PSS hybrid film, resulting in significant conductivity enhancement of the composite. Furthermore, the conductive PEDOT not only acted as a pillar between $\text{Ti}_3\text{C}_2\text{T}_x$ sheets to expose more electroactive surfaces and reduce ion diffusion pathways but also played a role as a conductive bridge to form multidimensional electronic transport channels for accelerating the electrochemical reaction process. As a result, the as-prepared H_2SO_4 -treated $\text{Ti}_3\text{C}_2\text{T}_x$ /PEDOT:PSS ($\text{Ti}_3\text{C}_2\text{T}_x$ /P-100-H) hybrid film exhibited 4.5-fold increase in the specific surface area and high volumetric capacitance of 1065 F cm^{-3} at 2 mV s^{-1} with superior rate performance in $1 \text{ M H}_2\text{SO}_4$ electrolyte. Especially, we assembled an asymmetric supercapacitor (ASC) with excellent flexibility based on a $\text{Ti}_3\text{C}_2\text{T}_x$ /P-100-H hybrid negative electrode and rGO film positive electrode, which delivered high energy density of 23 mW h cm^{-3} and high power density of 7659 mW cm^{-3} . Moreover, a simple luminous band was designed and powered by our two ASCs in series. The outstanding volumetric electrochemical performance and energy density of the ASC based on the flexible $\text{Ti}_3\text{C}_2\text{T}_x$ /P-100-H hybrid film electrode demonstrated its promising potential as a strong power source for small portable and wearable electronic devices.

Received 3rd November 2018,
Accepted 22nd December 2018

DOI: 10.1039/c8dt04374d

rsc.li/dalton

Introduction

High-performance supercapacitors with high power density and energy density as well as long cycle life are crucial for the development of innovative portable and wearable electronic devices.^{1,2} However, the currently commercialized supercapacitors cannot satisfy this requirement because they mainly use low-capacitance carbon materials as the negative electrode, which results in low energy density of the device.^{3,4} Thus,

exploring high-performance negative electrode materials, such as metal oxides and metal sulfides,^{5,6} has been the goal of researchers. In recent years, MXenes, a family of two-dimensional (2D) transition metal carbides and nitrides, have been widely studied for supercapacitors as negative electrode materials due to their suitable potential range and excellent properties such as metallic conductivity, hydrophilic surface and good elastic properties.^{7–12} Nevertheless, the restacking of MXene nanosheets (NSs) arising from the strong van der Waals interaction between adjacent MXene NSs largely compromises their available surface area and limits the electrochemical performance.^{13,14} Wedging spacers between the sheets is a straightforward strategy to alleviate this phenomenon and simultaneously increase the electrochemical properties. For example, metal cations (Li^+ , Na^+ , K^+ , NH_4^+ and Mg^{2+}),¹⁵ organic molecules (hydrazine molecule),¹⁶ carbon nanomaterials (onion-like carbon, carbon nanotubes and graphene),^{17,18} and metal oxides/sulfides (TiO_2 nanoparticles,¹⁹

^aCondensed Matter Science and Technology Institute, Department of Physics, Harbin Institute of Technology, Harbin 150001, People's Republic of China

^bKey Laboratory for Photonic and Electronic Bandgap Materials, Ministry of Education, School of Physics and Electronic Engineering, Harbin Normal University, Harbin 150025, People's Republic of China. E-mail: xtzhazhang@hotmail.com

^cDepartment of Chemistry and Chemical Biology, Cornell University, Ithaca, USA

†Electronic supplementary information (ESI) available. See DOI: 10.1039/c8dt04374d

MnO₂ nanosheets¹⁴ and MoS₂ nanosheets²⁰) are introduced between MXene nanosheets as interlayer spacers, which result in improved electrochemical performance *via* increase in the electrode/electrolyte interface areas and decrease in the ion diffusion length within the active materials. Beyond that, polymers are a special class of interlayer spacer materials. It has been proven that the combination of MXenes with polymers can enhance their electrochemical performance and render the hybrids with superior mechanical properties, which is necessary for the electrode materials of next-generation wearable and flexible supercapacitors. For instance, Ling *et al.* mixed Ti₃C₂T_x with electrically neutral polyvinyl alcohol (PVA) to produce Ti₃C₂T_x/PVA composites.²¹ The intercalation and confinement of the polymer between MXene flakes enhanced the cationic intercalation, offering remarkable volumetric capacitance of ~530 F cm⁻³ for the MXene/PVA-KOH composite film at 2 mV s⁻¹; moreover, this strategy also increased flexibility, exhibiting improved strength that was about four times larger than that of a pure Ti₃C₂T_x film by increasing the PVA loading to 60 wt%. Boota *et al.* demonstrated a facile strategy for the *in situ* polymerization of pyrrole confined between Ti₃C₂T_x layers, and the PPy/Ti₃C₂T_x composite yielded volumetric capacitance of ~1000 F cm⁻³.²² From a variety of polymers, poly(3,4-ethylenedioxythiophene) (PEDOT) is preferred due to its mechanical flexibility, low cost, and commercial availability.^{23,24} Compared with the *in situ* polymerization of a monomer on the surface of the Ti₃C₂T_x sheet, the method of directly mixing a PEDOT aqueous solution and Ti₃C₂T_x supernatant is much easier to operate and cheaper in industrial production. Clevios PH1000 is a commercially available aqueous dispersion of PEDOT with poly(styrenesulfonate) (PSS) as a dispersant. However, PSS is an insulator that impedes charge transport. Based on a previously reported method, we inferred that a strong acid treatment is the most effective and simple way to remove the insulating PSS and improve the conductivity of the film dramatically.²⁵ To the best of our knowledge, there are no reports on an H₂SO₄-treated Ti₃C₂T_x/PEDOT:PSS composite film electrode for supercapacitors, and the hybrid film is expected to be a high-performance negative electrode material.

In this study, a flexible H₂SO₄-treated Ti₃C₂T_x/PEDOT:PSS (Ti₃C₂T_x/P-H) hybrid film electrode was prepared by filtering the compound inks of Ti₃C₂T_x suspension and Clevios PH1000, followed by immersion in a concentrated H₂SO₄ solution. The optimal ratio of the Ti₃C₂T_x/P-100-H hybrid film electrode delivered ultrahigh volumetric capacitance of 1065 F cm⁻³ at 2 mV s⁻¹, good rate performance of 62% after increasing the scan rate by 50 times, and long-term cycling stability with an approximate decay rate of 0.002% per cycle over 10 000 cycles. Furthermore, we fabricated an asymmetric supercapacitor (ASC) based on a Ti₃C₂T_x/P-100-H hybrid film negative electrode and rGO film positive electrode using 1 M H₂SO₄ as the electrolyte. The device exhibited high energy density and power density (the maximum energy density of 23 mW h cm⁻³ and maximum power density of 7659 mW cm⁻³). A simple luminous band was lit by the ASC, suggesting its practicality for applications.

Experimental

Synthesis of Ti₃C₂T_x colloidal solution

One g Ti₃AlC₂ powder was added to a premixed solution of 1.56 g LiF and 20 mL HCl with continuous stirring at 38 °C for 48 h.^{26,27} Afterwards, the mixture was washed with 1 M HCl solution, 1 M LiCl solution and deionized water several times. The supernatant of Ti₃C₂T_x sheets was collected after centrifuging at 8000 rpm for 5 min.

Preparation of H₂SO₄-treated Ti₃C₂T_x/PEDOT:PSS (Ti₃C₂T_x/P-H) hybrid film

To synthesize the Ti₃C₂T_x/PEDOT:PSS hybrid film, Ti₃C₂T_x dispersions (1.5 mg mL⁻¹) and Clevios PH1000 were mixed and stirred for 1 h to achieve homogeneous inks. Then, the mixture was filtered through a PTFE membrane (0.22 μm pore size). Hybrid films with different ratios of Ti₃C₂T_x and PH1000 solutions were prepared and marked as Ti₃C₂T_x, Ti₃C₂T_x/P-50, Ti₃C₂T_x/P-100, and Ti₃C₂T_x/P-200; the detailed experimental parameters are listed in Table S1.† After soaking in concentrated H₂SO₄ for 24 h, these hybrid films were marked as Ti₃C₂T_x-H, Ti₃C₂T_x/P-50-H, Ti₃C₂T_x/P-100-H, and Ti₃C₂T_x/P-200-H. The PEDOT:PSS film was also prepared by filtering 2 ml PH1000 solution followed by soaking in H₂SO₄ for 24 h, and it was named as P-H.

Preparation of reduced graphene oxide (rGO) film

Graphite oxide was synthesized by a modified Hummers' method.²⁸ The GO film was obtained by filtering 5 ml GO solution (2 mg mL⁻¹), which was then immersed in a Teflon-lined stainless steel autoclave that contained 10 mL deionized water and 400 μL hydrazine hydrate (80%). Finally, the obtained rGO film was collected and dried after sealing the autoclave at 90 °C for 6 h in an electric oven.

Characterization

The morphology and chemical composition of samples were characterized by field-emission scanning electron microscopy (FE-SEM; SU70, Hitachi, Japan) and transmission electron microscopy (TEM; FEI, Tecnai TF20). The X-ray powder diffraction (XRD) spectra were collected on a Rigaku D/max2600 X-ray diffractometer. Raman spectra were characterized by a Micro-Raman spectrometer (J-Y; HR800, France) under an excitation wavelength of 488 nm. Fourier transform infrared (FT-IR) spectra were obtained using a Magna Model 560 FT-IR spectrometer with a resolution of 1 cm⁻¹. The nitrogen adsorption/desorption isotherms were obtained on an ASAP 2010 accelerated surface area and porosimetry instrument (Micromeritics). Zeta potential was measured using Malvern Zetasizer Nano ZS90new (USA).

Electrochemical measurements

Electrochemical measurements were conducted in 1 M H₂SO₄ electrolyte with a standard three-electrode system using a VMP3 electrochemical workstation (BioLogic, France). Samples with size of 1.0 × 0.5 cm², carbon rod and Ag/AgCl served as

the working, counter and reference electrodes, respectively. Electrochemical impedance spectroscopy (EIS) was conducted with an AC perturbation of 10 mV over a frequency range from 0.01 Hz to 100 kHz. In the case of the asymmetric supercapacitor device, we used the $\text{Ti}_3\text{C}_2\text{T}_x/\text{P-100-H}$ hybrid film as the negative electrode, a separator (PTFE, Shanghai Minglie Chemical Technology Co., Ltd), rGO film as the positive electrode and 1 M H_2SO_4 electrolyte. The energy density and power density of the ASC were calculated based on the volume of the active materials including the two working electrodes.

Results and discussion

To suppress the restacking of 2D $\text{Ti}_3\text{C}_2\text{T}_x$ NSs and further improve the electrochemical performance of the $\text{Ti}_3\text{C}_2\text{T}_x$ electrode, the conductive polymer PEDOT was introduced as a spacer between $\text{Ti}_3\text{C}_2\text{T}_x$ NSs. Fig. 1 schematically illustrates the procedure used to prepare H_2SO_4 -treated $\text{Ti}_3\text{C}_2\text{T}_x/\text{PEDOT:PSS}$ ($\text{Ti}_3\text{C}_2\text{T}_x/\text{P-H}$) hybrid film electrodes. The $\text{Ti}_3\text{C}_2\text{T}_x$ suspension and Clevios PH1000 aqueous solution are represented by green-black and dark blue colors, respectively. The surfaces of $\text{Ti}_3\text{C}_2\text{T}_x$ and PH1000 were both negatively charged with ζ -potentials of -20.9 mV and -73.5 mV (Fig. S1[†]), respectively. After mixing the two solutions, the electrostatic repulsion between $\text{Ti}_3\text{C}_2\text{T}_x$ and PH1000 helped maintain the stability of the colloidal mixture without apparent agglomeration. As reported previously, when treating PEDOT:PSS with concentrated H_2SO_4 , H^+ from H_2SO_4 can associate with PSS^- to form hydrophilic PSSH, which can be removed by washing.²⁵ After treatment, $\text{Ti}_3\text{C}_2\text{T}_x/\text{P-H}$ hybrid films were achieved. Interestingly, the hybrid film $\text{Ti}_3\text{C}_2\text{T}_x/\text{P-100-H}$ was found to exhibit the best electrochemical performance; therefore, characterizations of the morphology and structure for the optimum composition of $\text{Ti}_3\text{C}_2\text{T}_x/\text{P-100-H}$ were mainly addressed.

The as-prepared $\text{Ti}_3\text{C}_2\text{T}_x/\text{P-100-H}$ film exhibited excellent flexibility and could be folded or twisted many times without any structural degradation, as shown in Fig. 2a. Due to the

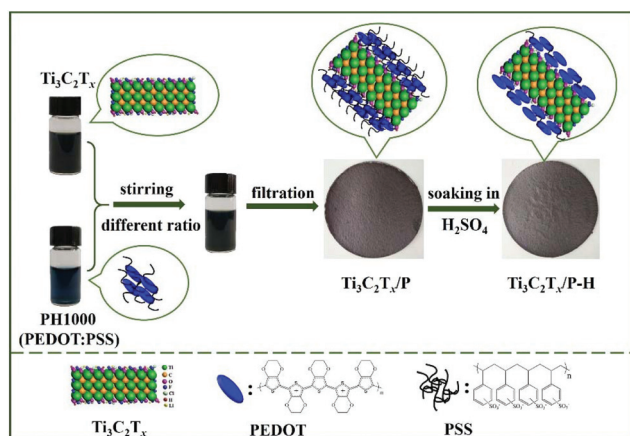


Fig. 1 Schematic illustration for the formation mechanism of $\text{Ti}_3\text{C}_2\text{T}_x/\text{P-H}$ hybrid film electrodes.

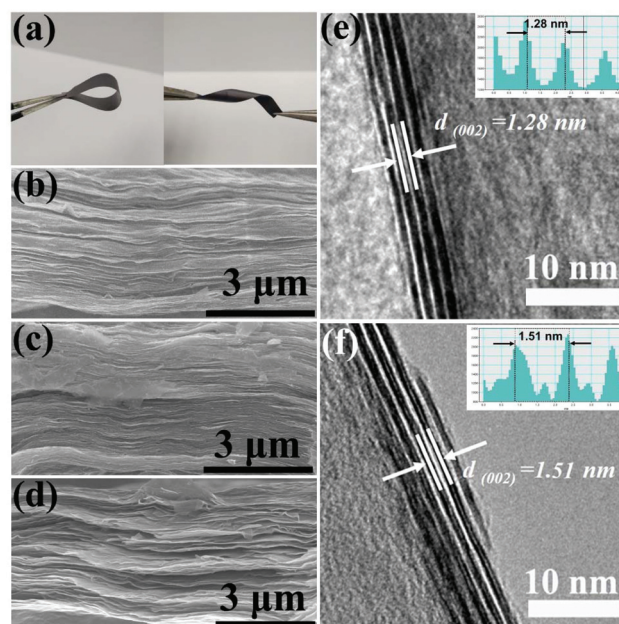


Fig. 2 (a) Digital images showing flexibility of the $\text{Ti}_3\text{C}_2\text{T}_x/\text{P-100-H}$ film; cross-section SEM images of (b) $\text{Ti}_3\text{C}_2\text{T}_x$, (c) $\text{Ti}_3\text{C}_2\text{T}_x/\text{P-100}$, and (d) $\text{Ti}_3\text{C}_2\text{T}_x/\text{P-100-H}$ films; HRTEM images of (e) $\text{Ti}_3\text{C}_2\text{T}_x$ and (f) $\text{Ti}_3\text{C}_2\text{T}_x/\text{P-100-H}$ films (inset is a profile plot of the calibration for measuring the spacing of $\text{Ti}_3\text{C}_2\text{T}_x$ NSs).

excellent mechanical flexibility of the $\text{Ti}_3\text{C}_2\text{T}_x/\text{P-100-H}$ hybrid film, it is suitable for use as the electrode material of next-generation wearable and flexible supercapacitors. Fig. 2b, c, and d show the cross-section SEM images of pure $\text{Ti}_3\text{C}_2\text{T}_x$, $\text{Ti}_3\text{C}_2\text{T}_x/\text{P-100}$, and $\text{Ti}_3\text{C}_2\text{T}_x/\text{P-100-H}$ films, respectively. The pristine $\text{Ti}_3\text{C}_2\text{T}_x$ film (Fig. 2b) showed a well-aligned layered structure and maintained the orderly stacked layers after concentrated H_2SO_4 treatment (Fig. S2[†]). When PH1000 was incorporated to form the $\text{Ti}_3\text{C}_2\text{T}_x/\text{P-100}$ film (Fig. 2c), it was found that there were less clear layer structures with closed edges over the entire film, which can be attributed to the alternating arrangement and interlocking of $\text{Ti}_3\text{C}_2\text{T}_x$ and PEDOT in the presence of PSS (Fig. S2b[†]). However, the $\text{Ti}_3\text{C}_2\text{T}_x/\text{P-100-H}$ film (Fig. 2d) was restored to an open-edged and much sparser layer structure after concentrated H_2SO_4 treatment, which indicated that the remaining PEDOT, left after partially removing PSS, as a spacer can effectively prevent the restacking of $\text{Ti}_3\text{C}_2\text{T}_x$ NSs and provide a higher accessible surface area. This speculation was further confirmed by the N_2 adsorption/desorption measurement (Fig. S3[†]). The $\text{Ti}_3\text{C}_2\text{T}_x/\text{P-100-H}$ film exhibited a specific surface area of $73.7 \text{ m}^2 \text{ g}^{-1}$, which was 4.5 times that of the restacked $\text{Ti}_3\text{C}_2\text{T}_x$ film ($16.2 \text{ m}^2 \text{ g}^{-1}$). The $\text{Ti}_3\text{C}_2\text{T}_x/\text{P-100-H}$ film with a more open accessible surface area provided excess active sites for electrochemical reactions. Thus, we deduce that the $\text{Ti}_3\text{C}_2\text{T}_x/\text{P-100-H}$ hybrid films can exhibit improved electrochemical performance.

To fully demonstrate the microstructure, Fig. 2e shows the high-resolution transmission electron microscopy (HRTEM) image of $\text{Ti}_3\text{C}_2\text{T}_x$; the single atom interlayer spacing of 12.8 \AA

(the inset of Fig. 2e) corresponds to the (002) plane of $\text{Ti}_3\text{C}_2\text{T}_x$. Compared with the observation for pure $\text{Ti}_3\text{C}_2\text{T}_x$ NSs, the intercalation of PEDOT:PSS layers can be clearly identified from the HRTEM image of the $\text{Ti}_3\text{C}_2\text{T}_x/\text{P-100}$ hybrid film (Fig. S2b†). In the profile plot of the calibration for measuring the spacing of $\text{Ti}_3\text{C}_2\text{T}_x$ layers, as shown in the inset of Fig. S2b,† there is a new periodic structure, which is reflected by a combination of a high peak and two low peaks, certifying the formation of alternating $\text{Ti}_3\text{C}_2\text{T}_x$ and PEDOT:PSS layers (Fig. S2b†). However, the periodic structure changes after concentrated H_2SO_4 treatment, which is reflected by a combination of a high peak and a low peak in the profile plot of the calibration, as shown in the inset of Fig. 2f. Thus, we speculated that most of the PSS is removed from the composite film after H_2SO_4 treatment. Besides, in the HRTEM image of the $\text{Ti}_3\text{C}_2\text{T}_x/\text{P-100-H}$ hybrid film shown in Fig. 2f, the interlayer spacing between $\text{Ti}_3\text{C}_2\text{T}_x$ layers of $\text{Ti}_3\text{C}_2\text{T}_x/\text{P-100-H}$ hybrid film is 15.1 Å, which is much larger than that of pure $\text{Ti}_3\text{C}_2\text{T}_x$, confirming the suppressive restacking of $\text{Ti}_3\text{C}_2\text{T}_x$ NSs. The diffusion and transport of electrolyte ions could be greatly promoted by the increased interlayer spacing, and the ion transport pathways for fast charge storage could be significantly improved by ordered morphologies of alternating $\text{Ti}_3\text{C}_2\text{T}_x$ and polymer layers.

To further illustrate the change in interlayer spacing observed by TEM, the XRD patterns of the as-synthesized films were obtained, as shown in Fig. 3a; Fig. 3b shows the corresponding enlarged XRD patterns. For the pure $\text{Ti}_3\text{C}_2\text{T}_x$ film, the existence of a clear characteristic (002) peak of $\text{Ti}_3\text{C}_2\text{T}_x$ at $2\theta = 6.9^\circ$ indicated the formation of a layered structure and the corresponding interlayer spacing value was calculated to be 12.8 Å. After mixing the $\text{Ti}_3\text{C}_2\text{T}_x$ suspension with PH1000 solu-

tion, the (002) peak position of $\text{Ti}_3\text{C}_2\text{T}_x$ exhibited a clear downshift from 6.9° to 6.2° , as shown in Fig. 3b, suggesting that PEDOT:PSS is intercalated between $\text{Ti}_3\text{C}_2\text{T}_x$ layers. After treatment by concentrated H_2SO_4 , the (002) peak position continued to downshift to 5.8° , and the corresponding interlayer spacing was ≈ 15.2 Å, which was consistent with the TEM observation (Fig. 2f). This shift may be attributed to water or proton intercalation. However, no diffraction peaks related to the PEDOT polymer backbone were distinguished in the XRD patterns of $\text{Ti}_3\text{C}_2\text{T}_x/\text{P-100}$ and $\text{Ti}_3\text{C}_2\text{T}_x/\text{P-100-H}$ hybrid films due to the amorphous crystal structure. The chemical structure of the synthesized $\text{Ti}_3\text{C}_2\text{T}_x/\text{P-100-H}$ hybrid film was further characterized using Raman and FT-IR spectra. In the Raman spectrum shown in Fig. 3c, the peaks at 1375 and 1576 cm^{-1} for the $\text{Ti}_3\text{C}_2\text{T}_x\text{-H}$ sample are characteristic of the D-mode and G-mode of graphitic carbon, which are attributed to exposed C on the surface of $\text{Ti}_3\text{C}_2\text{T}_x$. In the Raman spectrum of H_2SO_4 -treated PEDOT:PSS film (P-H), Raman bands at 994, 1260, 1370, 1429 and 1520 cm^{-1} correspond to oxyethylene ring deformation, $\text{C}_\alpha\text{-C}_\alpha$ inter-ring stretching vibrations, antisymmetric $\text{C}_\beta\text{-C}_\beta$ stretching deformations, symmetric stretching mode of the aromatic $\text{C}=\text{C}$ band, and antisymmetric $\text{C}_\alpha\text{-C}_\alpha$ stretching deformations.^{29,30} In addition, the Raman bands between 1400 and 1600 cm^{-1} become narrower and the intensities of these peaks decrease after concentrated H_2SO_4 treatment, as shown in Fig. S4,† which confirms that most of the PSS is removed.^{31,32} The signature peaks for PEDOT and $\text{Ti}_3\text{C}_2\text{T}_x$ were also found for the $\text{Ti}_3\text{C}_2\text{T}_x/\text{P-100-H}$ hybrid film, demonstrating that PEDOT was successfully intercalated between $\text{Ti}_3\text{C}_2\text{T}_x$ NSs. This result was further corroborated by the FT-IR spectra, as displayed in Fig. 3d. It can be seen that

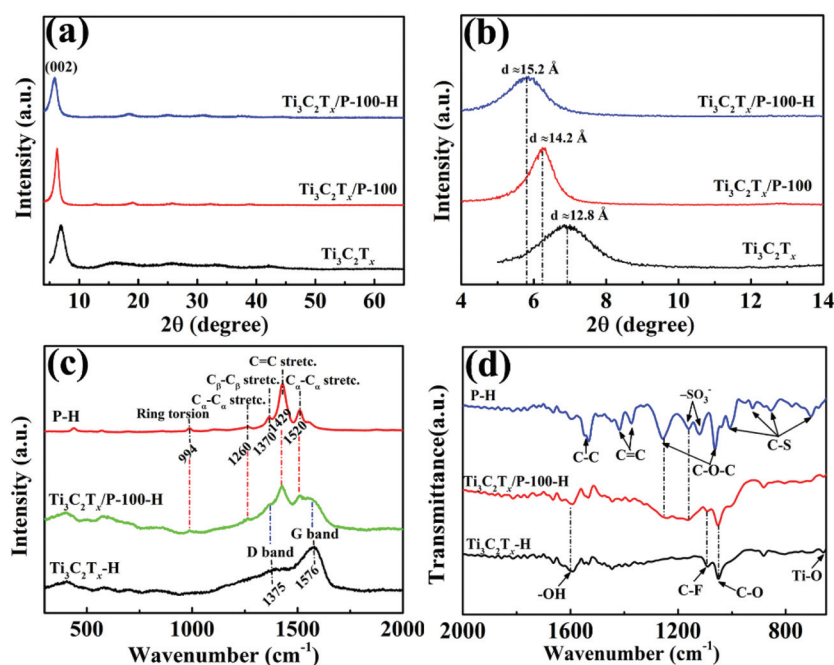


Fig. 3 (a) XRD patterns of $\text{Ti}_3\text{C}_2\text{T}_x$, $\text{Ti}_3\text{C}_2\text{T}_x/\text{P-100}$ and $\text{Ti}_3\text{C}_2\text{T}_x/\text{P-100-H}$ and (b) the corresponding enlarged XRD patterns, (c) Raman spectra and (d) FTIR spectra of $\text{Ti}_3\text{C}_2\text{T}_x\text{-H}$, $\text{Ti}_3\text{C}_2\text{T}_x/\text{P-100-H}$ and P-H films.

C–O ($\sim 1051\text{ cm}^{-1}$), C–F ($\sim 1090\text{ cm}^{-1}$) and –OH ($\sim 1600\text{ cm}^{-1}$) groups exist in $\text{Ti}_3\text{C}_2\text{T}_x\text{-H}$;³³ the peak at 665 cm^{-1} is attributed to the vibration of the Ti–O bond.³⁴ For H_2SO_4 -treated PEDOT: PSS film (P-H), the FT-IR bands at 1530 , 1420 cm^{-1} and 1370 cm^{-1} were mainly due to the C–C and C=C stretchings of the quinoidal structure of the thiophene rings.^{35,36} The bands at 1258 and 1063 cm^{-1} were assigned to the C–O–C bond stretching in the ethylene dioxide units.^{24,36} The C–S stretching mode exhibited IR bands at 1006 , 922 , 856 and 706 cm^{-1} .^{35,36} The hybrid $\text{Ti}_3\text{C}_2\text{T}_x/\text{P-100-H}$ film exhibited a combined character of the PEDOT and $\text{Ti}_3\text{C}_2\text{T}_x$ spectra, suggesting the intercalation of PEDOT between $\text{Ti}_3\text{C}_2\text{T}_x$ layers. The above SEM, TEM, XRD, Raman and FT-IR results suggest that PEDOT has been successfully intercalated between $\text{Ti}_3\text{C}_2\text{T}_x$ NSs. The interlayered polymer can expand the space between $\text{Ti}_3\text{C}_2\text{T}_x$ NSs and effectively hinder the re-stacking phenomenon, which is beneficial to expose more active sites and increase electron transfer and ion diffusion into the electrode materials more efficiently.

The electrochemical behavior of the $\text{Ti}_3\text{C}_2\text{T}_x/\text{P-100-H}$ hybrid film was studied, as shown in Fig. 4. For comparison, all the

electrode materials were controlled with the same mass loading of $\text{Ti}_3\text{C}_2\text{T}_x$ per unit area. CV curves for $\text{Ti}_3\text{C}_2\text{T}_x/\text{P-100-H}$ hybrid film electrode are shown in Fig. 4a; slight variations in the shapes of the CV curves indicate high electron and electrolyte ion mobility in the hybrid film. Continuous change in the titanium oxidation state during the charge/discharge process in H_2SO_4 electrolyte led to no distinct redox peaks in the CV curves.³⁷ GCD curves in Fig. 4b exhibit a linear symmetrical charge–discharge profile with no noticeable voltage drop (iR drop), implying the high reversibility of the redox reactions and low equivalent series resistance in the $\text{Ti}_3\text{C}_2\text{T}_x/\text{P-100-H}$ hybrid film electrode. As control groups, the electrochemical performances of $\text{Ti}_3\text{C}_2\text{T}_x$ and $\text{Ti}_3\text{C}_2\text{T}_x/\text{P-100}$ film electrodes are shown in Fig. S5.† The relationships of the volumetric capacitances and specific capacitance as a function of scan rates for the as-prepared samples are shown in Fig. 4c and Fig. S6.† In contrast, the pure $\text{Ti}_3\text{C}_2\text{T}_x$ film electrode showed volumetric capacitance of 952 F cm^{-3} (241 F g^{-1}) at 2 mV s^{-1} and rate performance of 58% as the scan rate increased to 100 mV s^{-1} . The effect of H_2SO_4 treatment on the electrochemical performance of the $\text{Ti}_3\text{C}_2\text{T}_x$ film electrode was almost negligible (Fig. S7†).

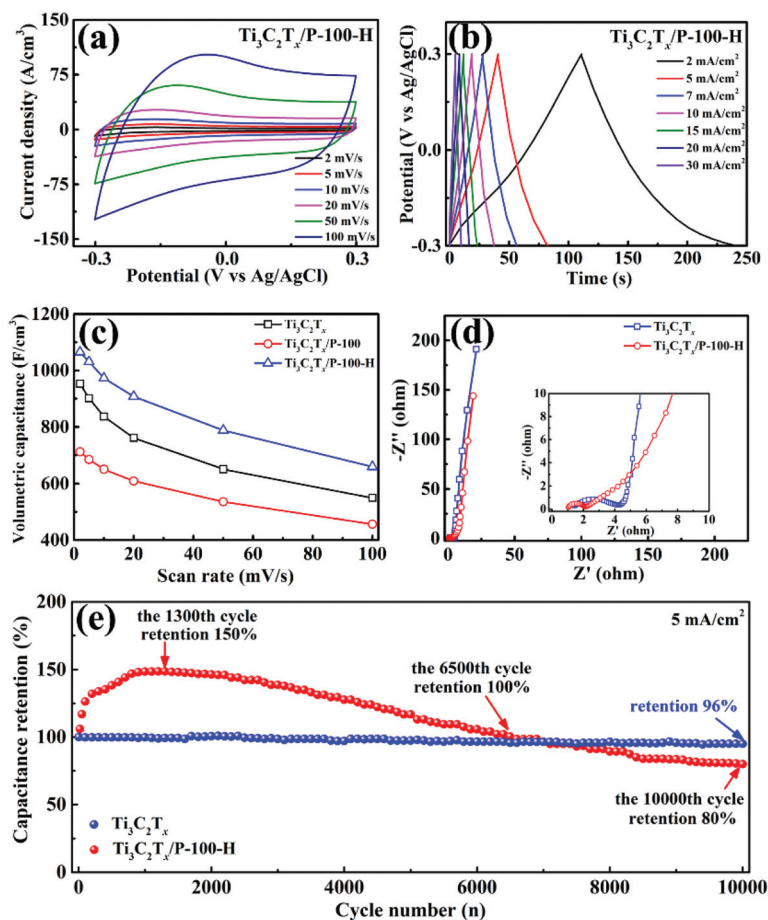


Fig. 4 (a) CV curves and (b) GCD curves of $\text{Ti}_3\text{C}_2\text{T}_x/\text{P-100-H}$ hybrid film electrode at different scan rates and current densities. (c) Volumetric capacitance of the as-prepared hybrid film electrodes as a function of scan rate. (d) Nyquist plots of the as-prepared hybrid film electrodes; inset shows the magnified high-frequency region. (e) Cycling stability of pure $\text{Ti}_3\text{C}_2\text{T}_x$ and $\text{Ti}_3\text{C}_2\text{T}_x/\text{P-100-H}$ hybrid film electrodes at a current density of 5 mA cm^{-2} .

Besides, the P-H electrode exhibited poor electrochemical performance of only 106 F cm^{-3} at 2 mV s^{-1} (Fig. S8†). After mixing PH1000 with $\text{Ti}_3\text{C}_2\text{T}_x$ to form the $\text{Ti}_3\text{C}_2\text{T}_x/\text{P-100}$ film, the volumetric capacitance decreased dramatically to 712 F cm^{-3} (216 F g^{-1}) at 2 mV s^{-1} (Fig. 4c), which can be attributed to the closed surface of the $\text{Ti}_3\text{C}_2\text{T}_x/\text{P-100}$ film, as shown by the SEM results (Fig. 2c). However, after concentrated H_2SO_4 treatment, the volumetric capacitance of $\text{Ti}_3\text{C}_2\text{T}_x/\text{P-100-H}$ film electrode significantly improved to 1065 F cm^{-3} (286 F g^{-1}) at 2 mV s^{-1} , but it exhibited lower density (3.72 g cm^{-3}) compared with the pure $\text{Ti}_3\text{C}_2\text{T}_x$ film (3.95 g cm^{-3}) (Table S1†). The volumetric capacitance was higher than those of most previously reported Ti_3C_2 -based materials such as the few-layer $\text{Ti}_3\text{C}_2\text{T}_x$ film (350 F cm^{-3} , 1 M KOH),¹⁵ PPy/ $\text{Ti}_3\text{C}_2\text{T}_x$ film (1000 F cm^{-3} , $1 \text{ M H}_2\text{SO}_4$),²² sandwich-like $\text{Ti}_3\text{C}_2\text{T}_x/\text{SWCNT}$ film (390 F cm^{-3} , $1 \text{ M H}_2\text{SO}_4$),¹⁷ $\text{Ti}_3\text{C}_2\text{T}_x/\text{PVA}$ film (528 F cm^{-3} , 1 M KOH),²¹ $\text{Ti}_3\text{C}_2\text{T}_x/\text{rGO}$ film (1040 F cm^{-3} , $3 \text{ M H}_2\text{SO}_4$),¹³ and $\text{Ti}_3\text{C}_2\text{T}_x$ hydrogels (1500 F cm^{-3} , $3 \text{ M H}_2\text{SO}_4$).³⁸ More detailed comparison results are shown in Table S2.† Simultaneously, the $\text{Ti}_3\text{C}_2\text{T}_x/\text{P-100-H}$ film electrode exhibited increased rate performance of 62%, which may be due to PEDOT intercalated between $\text{Ti}_3\text{C}_2\text{T}_x$ NSs, providing multidimensional conductive channels for charge transfer. This speculation can be further confirmed by EIS shown in Fig. 4d. The Nyquist curves are composed of a high-frequency arc region and a low-frequency line region. The low-frequency lines of the $\text{Ti}_3\text{C}_2\text{T}_x$ and $\text{Ti}_3\text{C}_2\text{T}_x/\text{P-100-H}$ film electrodes are almost parallel to the y-axis, indicating an ideal capacitive behavior. The equivalent series resistance (ESR) values, intercept on Re (Z) in the high-frequency region, for $\text{Ti}_3\text{C}_2\text{T}_x$ and $\text{Ti}_3\text{C}_2\text{T}_x/\text{P-100-H}$ were $1.3 \text{ } \Omega$ and $1.0 \text{ } \Omega$, respectively, as shown in the enlarged view inset of Fig. 2e, indicating improvement in conductivity. Furthermore, R_{ct} (charge transfer resistance) of $\text{Ti}_3\text{C}_2\text{T}_x/\text{P-100-H}$ film electrode reflected by the arc radius in the high-frequency region was much smaller than that of $\text{Ti}_3\text{C}_2\text{T}_x$, suggesting an increase in ion accessibility, reduction of ion diffusion distances and improvement in the electron transfer rate. Long-term cycling stability is an important fundamental property for supercapacitors. The cycling life of the $\text{Ti}_3\text{C}_2\text{T}_x/\text{P-100-H}$ film electrode was evaluated through GCD measurements at a current density of 5 mA cm^{-2} , as shown in Fig. 4e. The capacitance of the $\text{Ti}_3\text{C}_2\text{T}_x$ electrode maintained 96% of its initial value after 10 000 cycles; however, interestingly, we found that the capacitance retention of the $\text{Ti}_3\text{C}_2\text{T}_x/\text{P-100-H}$ film electrode first increased to 150% of the initial value at the 1300th cycle due to the self-activation process, then reached the initial value at the 6500th cycle, and finally decayed to 80% after 10 000 cycles, corresponding to an approximate decay rate of 0.002% per cycle. Generally, PEDOT can usually accommodate large volumetric expansion and shrinkage during the charge/discharge process.³⁹ We speculated that for the $\text{Ti}_3\text{C}_2\text{T}_x/\text{P-100-H}$ film electrode, the PEDOT acted as a spacer to hinder the restacking of $\text{Ti}_3\text{C}_2\text{T}_x$ NSs, and $\text{Ti}_3\text{C}_2\text{T}_x$ NSs could effectively buffer the volume change of PEDOT. In agreement with this, the activation of this electrode required a much longer time up to 1300 cycles with increase in capacitance, thus increasing

the electrochemical durability beyond thousands of cycles. The influence of the amount of PEDOT in the hybrid film electrode was also examined (Fig. S9 and S10†). It was found that decreasing or increasing the mass loading of PEDOT resulted in worse electrochemical properties; this could be because decreasing the content of PEDOT decreases the interlayer spacing (Fig. S11†), whereas increasing the content of PEDOT with poor electrochemical performance results in reduced overall electrochemical properties of the hybrid electrode. Combining the above analyses, the superior performance of the hybrid $\text{Ti}_3\text{C}_2\text{T}_x/\text{P-100-H}$ electrode can be attributed to the following reasons: (i) the effective suppression of restacking of $\text{Ti}_3\text{C}_2\text{T}_x$ NSs and the increase in interlayer spacing improve accessibility of the ions due to pillaring of PEDOT; (ii) the enhancement in the exposed electroactive surface and the reduction in the ion diffusion pathway facilitate electron transfer and ion diffusion to promote the electrochemical reaction of $\text{Ti}_3\text{C}_2\text{T}_x$; (iii) the conductive polymer intercalated between $\text{Ti}_3\text{C}_2\text{T}_x$ NSs can form multidimensional pathways for electron transport to accelerate the electrochemical reaction process. Therefore, the hybrid $\text{Ti}_3\text{C}_2\text{T}_x/\text{P-100-H}$ electrode shows promising application prospects for a supercapacitor.

Based on previously reported theoretical analysis and experimental results, the total electrochemical stored charge of $\text{Ti}_3\text{C}_2\text{T}_x$ can be separated into three fractions: (1) the faradaic contribution from the slow H^+ ion insertion process limited by ion diffusion, (2) the faradaic contribution from the fast charge-transfer process at the surfaces originating from continuous change in the titanium oxidation state, which is also referred to as pseudocapacitance, and (3) the nonfaradaic contribution from the fast electric double layer effect at the surfaces.⁴⁰ Electrochemical analysis of different kinetic responses promotes a better understanding of the charge/discharge mechanism of the $\text{Ti}_3\text{C}_2\text{T}_x/\text{P-100-H}$ hybrid film electrode.

The fast surface-reaction process and the slower diffusion-controlled process can be distinguished with the Trasatti's method.⁴¹ To estimate the surface capacitance, the charge is extrapolated to an infinitely fast scan rate by plotting charge vs. $\nu^{-1/2}$. As shown in Fig. 5a, when $\nu \rightarrow \infty$, the contribution from the diffusion-controlled process is eliminated, and the y-intercept is the surface charge contribution (q_s). Furthermore, the maximum total charge (q_t) can be obtained at an infinitely slow scan rate. In Fig. 5b, when $\nu \rightarrow 0$, the y-intercept is q_t^{-1} and can be acquired by plotting q^{-1} vs. $\nu^{1/2}$. As a consequence, the surface capacitance and total capacitance of $\text{Ti}_3\text{C}_2\text{T}_x/\text{P-100-H}$ hybrid film electrode were calculated to be 864.8 and 1216.5 F cm^{-3} , which were higher than those of $\text{Ti}_3\text{C}_2\text{T}_x$ (705.0 and 1096.5 F cm^{-3}). The increased surface capacitance of the $\text{Ti}_3\text{C}_2\text{T}_x/\text{P-100-H}$ electrode could be attributed to PEDOT acting as a spacer, which prevented the restacking of $\text{Ti}_3\text{C}_2\text{T}_x$ NSs effectively, increased interlayer spacing, and provided a higher accessible surface area, as demonstrated by the results of SEM, XRD and BET analyses. Importantly, the surface capacitance for the $\text{Ti}_3\text{C}_2\text{T}_x/\text{P-100-H}$ electrode was predicted to be 71.1% of the total capacitance, which was 6.8% more than that of $\text{Ti}_3\text{C}_2\text{T}_x$ (64.3%) (Fig. 5c). This result

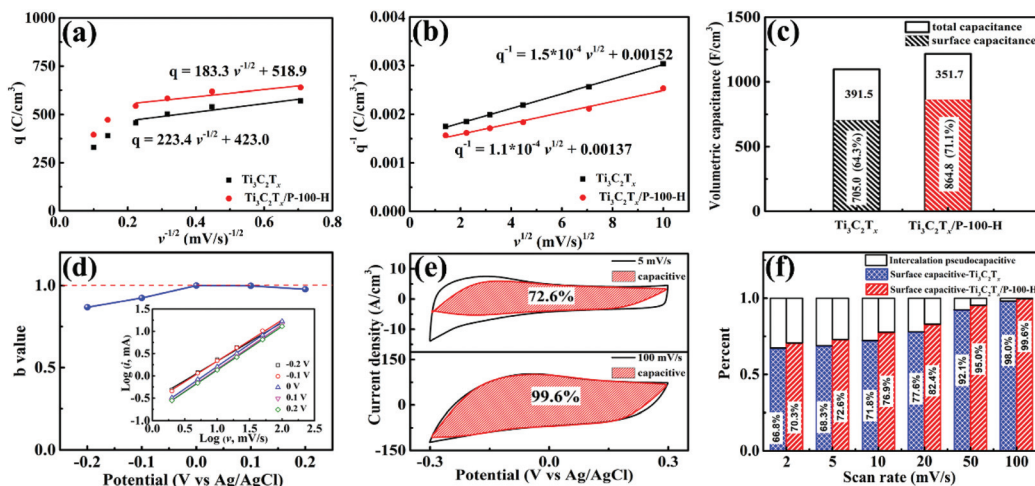


Fig. 5 (a) Stored charge (q) versus inverse of square root of the scan rate (v), (b) inverse of the stored charge versus the square root of the scan rate, (c) Trasatti's method of deconvoluting charge storage contributions, (d) b values plotted against voltages (inset: current response plotted against scan rate at different voltages), (e) capacitive contribution to charge storage at scan rates of 5 and 100 mV s^{-1} , (f) percentage of capacitance contribution at different scan rates.

explains the reason for the improvement in the rate performance of the $\text{Ti}_3\text{C}_2\text{T}_x/\text{P-100-H}$ electrode from the kinetics. The Trasatti's method indicated that $\text{Ti}_3\text{C}_2\text{T}_x/\text{P-100-H}$ facilitated a faster electrochemical reaction, resulting in both higher overall capacitance and higher contribution from the v -dependent charge, which included the contribution of the electrical double layer and all fast faradaic reactions that are not diffusion-limited. During the charging and discharging process, the current response rate to the surface-reaction was much faster than that to the H^+ ion insertion process limited by ion diffusion. Therefore, the higher the surface capacitance contribution of the electrode, the faster the current response speed, and the better the rate performance. This result provides a new solution for designing electrode materials having ultra-high rate performance.

To deeply investigate the charge storage and ion transport mechanism of $\text{Ti}_3\text{C}_2\text{T}_x/\text{P-100-H}$, the surface-reaction contribution and diffusion-controlled contribution of the total capacitance were further analyzed.⁴¹ Because the linear relationships between the response current and scan are $i_s \rightarrow v$ and $i_d \rightarrow v^{1/2}$ corresponding to the surface-reaction and diffusion-controlled processes, a general expression can be defined as eqn (1):

$$i = i_s + i_d = av^b \quad (1)$$

$$\log i = \log a + b \log v \quad (2)$$

Here, i is the current, a and b are variable parameters, and b -values can be determined from the slope of the plot of $\log i$ vs. $\log v$. Ideally, the exponent b will have values of $b = 0.5$ for the diffusion-controlled process and $b = 1$ for a surface reaction. In Fig. 5d, the b -values of $\text{Ti}_3\text{C}_2\text{T}_x/\text{P-100-H}$ dependent on different potentials are in the range of 0.85–1, indicating that the kinetics of $\text{Ti}_3\text{C}_2\text{T}_x/\text{P-100-H}$ was predominantly surface-

controlled. To determine the ratios of the capacitive contribution quantitatively, Dunn's method was introduced. This method deconvolutes the surface-reaction and diffusion-controlled contributions to current at a given voltage, i (V), based on the following equation:

$$i(V) = k_1v + k_2v^{1/2} \quad (3)$$

$$\frac{i(V)}{v^{1/2}} = k_1v^{1/2} + k_2 \quad (4)$$

Here, i (V), k_1v , $k_2v^{1/2}$ and v are the current at a fixed potential, surface-reaction and diffusion-controlled currents, and scan rate. Thus, by determining k_1 and k_2 , we can quantify the fraction of the current due to each of these contributions. Furthermore, the ratios of capacitive contribution can be quantitatively determined by comparing the shaded area with the total stored charge (Fig. 5e). It was found that the surface-reaction capacitive contribution of the $\text{Ti}_3\text{C}_2\text{T}_x/\text{P-100-H}$ electrode increased from 70.3% to 99.6%, as can be seen in Fig. 5f. Moreover, the surface-reaction capacitive contribution of the $\text{Ti}_3\text{C}_2\text{T}_x/\text{P-100-H}$ electrode was larger than that of $\text{Ti}_3\text{C}_2\text{T}_x$, which was consistent with the result calculated using the Trasatti's method. The increase in surface-reaction capacitive contribution can be attributed to the larger exposed active surface area, faster electron transfer and shorter ion diffusion length, which can explain why $\text{Ti}_3\text{C}_2\text{T}_x/\text{P-100-H}$ has high rate performance.

ASC and two ASC units are connected in series or in parallel, (i) a simple luminous band powered by two $\text{Ti}_3\text{C}_2\text{T}_x/\text{P-100-H}/\text{rGO}$ ASCs in series.

To extend the working voltage and increase the energy density, we assembled asymmetric supercapacitors (ASC) by using the $\text{Ti}_3\text{C}_2\text{T}_x/\text{P-100-H}$ hybrid film electrode as the negative electrode and the rGO film as the positive electrode (Fig. 6a).

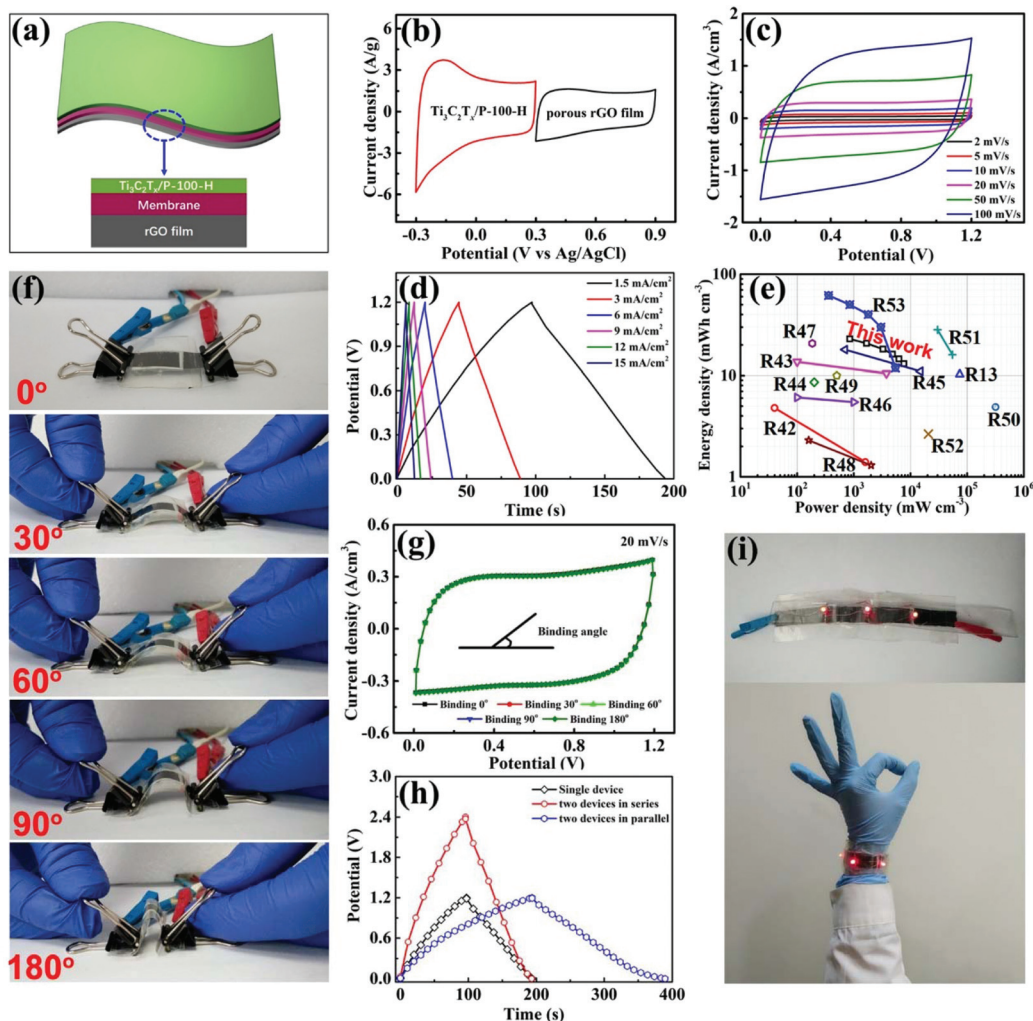


Fig. 6 (a) Schematic illustration for the assembled $\text{Ti}_3\text{C}_2\text{T}_x/\text{P-100-H}/\text{rGO}$ ASC, (b) CV curves obtained for $\text{Ti}_3\text{C}_2\text{T}_x/\text{P-100-H}$ and rGO electrodes at a scan rate of 10 mV s^{-1} , (c) CV curves and (d) GCD curves of ASC at different scan rates and current densities, (e) Ragone plots of ASC. The values reported for other ASCs are added for comparison, (f) pictures and (g) CV curves of the ASC measured at different bent conditions, (h) GCD curves obtained at a current density of 1.5 mA cm^{-2} for a single.

The rGO film (positive electrode) was selected due to its flexibility, good conductivity, high chemical stability and a matching potential application range with $\text{Ti}_3\text{C}_2\text{T}_x/\text{P-100-H}$. The as-prepared rGO film was characterized, as shown in Fig. S12.† In Fig. 6a, the working potential of $\text{Ti}_3\text{C}_2\text{T}_x/\text{P-100-H}$ is from -0.3 to 0.3 V , whereas the rGO film operates in a potential window from 0.3 to 0.9 V , which can enable effective cell voltage of up to 1.2 V . Fig. 6c presents the CV curves of flexible $\text{Ti}_3\text{C}_2\text{T}_x/\text{P-100-H}/\text{rGO}$ ASC at various scan rates. Clearly, the assembled ASC exhibits rectangular CV curves even at a high scan rate of 100 mV s^{-1} , indicating an ideal capacitive behavior and fast charge–discharge properties. In addition, the GCD curves of ASC (Fig. 6d) are linear slopes and the triangle shape corroborates the fast charge–discharge properties; the GCD curves are consistent with the CV curves. The ASC exhibited high volumetric capacitance of 117 F cm^{-3} calculated from GCD curve at 1.5 mA cm^{-2} and capacitance retention to 69.9% at

15 mA cm^{-2} . In Fig. 6e, we compare the volumetric power and energy densities of $\text{Ti}_3\text{C}_2\text{T}_x/\text{P-100-H}/\text{rGO}$ ASC to those of other supercapacitors reported previously. $\text{Ti}_3\text{C}_2\text{T}_x/\text{P-100-H}/\text{rGO}$ ASC delivered high energy density of 23 mW h cm^{-3} and high power density of 7659 mW cm^{-3} , which were closely comparable with or in some cases much higher than those of previously reported Ti_3C_2 -based supercapacitors and graphene-based supercapacitors: $\text{Ti}_3\text{C}_2/\text{rGO}$ (8.6 mW h cm^{-3} , 200 mW cm^{-3}),⁴⁴ $\text{PPy}/\text{l-Ti}_3\text{C}_2$ symmetric SC (10 mW h cm^{-3} , 500 mW cm^{-3}),⁴⁹ GO film//3D-DG@ MnO_2 ($28.2 \text{ mW h cm}^{-3}$, $30\,000 \text{ mW cm}^{-3}$),⁵² *etc.*,^{13,42,43,45–48,50,51,53} as listed in Table S3.† These results imply that the $\text{Ti}_3\text{C}_2\text{T}_x/\text{P-100-H}$ film electrode is expected to be a highly promising candidate for application as the negative electrode in high-performance energy storage systems.

To evaluate the potential use of the developed energy storage devices in flexible and wearable electronics, in addition

to the good performance in the relaxed state, the performances under different bending angles were characterized, as shown in Fig. 6f. According to the CV curves in Fig. 6g, no significant change in the integrated area of the CV curves is observed under bending, indicating the excellent flexibility of $\text{Ti}_3\text{C}_2\text{T}_x/\text{P-100-H}/\text{rGO}$ ASC. To build integration patterns, the same $\text{Ti}_3\text{C}_2\text{T}_x/\text{P-100-H}/\text{rGO}$ ASCs were connected in series or in parallel for practical applications. The GCD curves of two ASCs connected in parallel exhibit a discharge time about twice that of each single ASC at the same current density, as shown in Fig. 6h. As expected, the voltage window of two ASCs connected in series could reach 2.4 V, maintaining the same charging/discharging time; a simple luminous band that can be worn by fans at a concert or worn by traffic police to direct traffic using gesture signals at night was designed and powered by our two $\text{Ti}_3\text{C}_2\text{T}_x/\text{P-100-H}/\text{rGO}$ ASCs in series. After being charged, the serial-connected ASCs could drive the luminous band for about five minutes, as shown in Fig. 6i and Fig. S13,† which indicated that $\text{Ti}_3\text{C}_2\text{T}_x/\text{P-100-H}/\text{rGO}$ ASC has excellent application prospects in real life.

Conclusions

In summary, we developed a simple and effective strategy to produce a $\text{Ti}_3\text{C}_2\text{T}_x/\text{polymer}$ hybrid film electrode *via* filtering $\text{Ti}_3\text{C}_2\text{T}_x/\text{PH1000}$ compound inks, followed by H_2SO_4 treatment. The resulting flexible self-supporting $\text{Ti}_3\text{C}_2\text{T}_x/\text{P-100-H}$ film electrode exhibited high volumetric capacitance of 1065 F cm^{-3} at 2 mV s^{-1} and superior rate performance (62% retention after increasing scan rate by 50 times) in $1 \text{ M H}_2\text{SO}_4$ electrolyte. Such excellent electrochemical performance was observed because PEDOT acted as a pillar between $\text{Ti}_3\text{C}_2\text{T}_x$ NSs to expose more electroactive surfaces and reduce ion diffusion pathway; it also acted as the conductive bridge to form multi-dimensional electronic transport channels for accelerating the electrochemical reaction process. Moreover, an asymmetric supercapacitor, $\text{Ti}_3\text{C}_2\text{T}_x/\text{P-100-H}/\text{rGO}$, with excellent flexibility was assembled, which delivered high energy density of 23 mWh cm^{-3} and high power density of 7659 mW cm^{-3} . Furthermore, a simple luminous band was designed and powered by our two $\text{Ti}_3\text{C}_2\text{T}_x/\text{P-100-H}/\text{rGO}$ ASCs connected in series. Integrated ASCs demonstrated great potential for the development of portable/wearable electronics.

Conflicts of interest

There are no conflicts to declare.

Acknowledgements

This work was partially supported by the National Natural Science Foundation of China (No. 51472066, 51872068 and 51772069) and Natural Science Foundation of Heilongjiang Province, China (E2018051).

Notes and references

- 1 Y. G. Wang, Y. F. Song and Y. Y. Xia, *Chem. Soc. Rev.*, 2016, **45**, 5925.
- 2 L. Huang, D. Santiago, P. Loyselle and L. M. Dai, *Small*, 2018, 1800879.
- 3 Y. L. Shao, M. F. El-Kady, J. Y. Sun, Y. G. Li, Q. H. Zhang, M. F. Zhu, H. Z. Wang, B. Dunn and R. B. Kaner, *Chem. Rev.*, 2018, **118**, 9233.
- 4 A. Borenstein, O. Hanna, R. Attias, S. Luski, T. Brousse and D. Aurbach, *J. Mater. Chem. A*, 2017, **5**, 12653.
- 5 L. Li, X. T. Zhang, Z. G. Zhang, M. Y. Zhang, L. J. Cong, Y. Pan and S. Y. Lin, *J. Mater. Chem. A*, 2016, **4**, 16635.
- 6 X. Lei, K. Yu, R. J. Qi and Z. Q. Zhu, *Chem. Eng. J.*, 2018, **347**, 607.
- 7 B. Anasori, M. R. Lukatskaya and Y. Gogotsi, *Nat. Rev. Mater.*, 2017, **2**, 16098.
- 8 X. Zhang, Z. H. Zhang and Z. Zhou, *J. Energy Chem.*, 2018, **27**, 73.
- 9 S. J. Sun, C. Liao, A. M. Hafez, H. L. Zhu and S. P. Wu, *Chem. Eng. J.*, 2018, **338**, 27.
- 10 M. Naguib, M. Kurtoglu, V. Presser, J. Lu, J. J. Niu, M. Heon, L. Hultman, Y. Gogotsi and M. W. Barsoum, *Adv. Mater.*, 2011, **23**, 4248.
- 11 M. Naguib, J. Halim, J. Lu, K. Cook, L. Hultman, Y. Gogotsi and M. W. Barsoum, *J. Am. Chem. Soc.*, 2013, **135**, 15966.
- 12 O. Mashtalir, M. Naguib, V. N. Mochalin, Y. Dall'Agnese, M. Heon, M. W. Barsoum and Y. Gogotsi, *Nat. Commun.*, 2013, **4**, 1716.
- 13 J. Yan, C. E. Ren, K. Maleski, C. B. Hatter, B. Anasori, P. Urbankowski, A. Sarycheva and Y. Gogotsi, *Adv. Funct. Mater.*, 2017, **27**, 1701264.
- 14 W. H. Liu, Z. Q. Wang, Y. L. Su, Q. W. Li, Z. G. Zhao and F. X. Geng, *Adv. Energy Mater.*, 2017, **7**, 1602834.
- 15 M. R. Lukatskaya, O. Mashtalir, C. E. Ren, Y. D. Agnese, P. Rozier, P. L. Taberna, M. Naguib and P. Simon, *Science*, 2013, **341**, 1502.
- 16 O. Mashtalir, M. R. Lukatskaya, A. I. Kolesnikov, E. Raymundo-Piñero, M. Naguib, M. W. Barsoum and Y. Gogotsi, *Nanoscale*, 2016, **8**, 9128.
- 17 M. Q. Zhao, C. E. Ren, Z. Ling, M. R. Lukatskaya, C. F. Zhang, K. L. V. Aken, M. W. Barsoum and Y. Gogotsi, *Adv. Mater.*, 2015, **27**, 339.
- 18 Q. S. Fu, X. Y. Wang, N. Zhang, J. Wen, L. Li, H. Gao and X. T. Zhang, *J. Colloid Interface Sci.*, 2018, **511**, 128.
- 19 A. Shahzad, K. Rasool, M. Nawaz, W. Miran, J. Jang, M. Moztahida, K. A. Mahmoud and D. S. Lee, *Chem. Eng. J.*, 2018, **349**, 748.
- 20 X. H. Wu, Z. Y. Wang, M. Z. Yu, L. Y. Xiu and J. S. Qiu, *Adv. Mater.*, 2017, **29**, 1607017.
- 21 Z. Ling, C. E. Ren, M. Q. Zhao, J. Yang, J. M. Giammarco, J. S. Qiu, M. W. Barsoum and Y. Gogotsi, *Proc. Natl. Acad. Sci. U. S. A.*, 2014, **111**, 16676.
- 22 M. Boota, B. Anasori, C. Voigt, M. Q. Zhao, M. W. Barsoum and Y. Gogotsi, *Adv. Mater.*, 2016, **28**, 1517.

- 23 M. Zhang, W. J. Yuan, B. W. Yao, C. Li and G. Q. Shi, *ACS Appl. Mater. Interfaces*, 2014, **6**, 3587.
- 24 Y. Q. Liu, B. Weng, J. M. Razal, Q. Xu, C. Zhao, Y. Y. Hou, S. Seyedin, R. Jalili, G. G. Wallace and J. Chen, *Sci. Rep.*, 2015, **5**, 17045.
- 25 Y. J. Xia, K. Sun and J. Y. Ouyang, *Adv. Mater.*, 2012, **24**, 2436.
- 26 X. Y. Wang, Q. S. Fu, J. Wen, X. Z. Ma, C. C. Zhu, X. T. Zhang and D. P. Qi, *Nanoscale*, 2018, **10**, 20828.
- 27 L. Li, M. Y. Zhang, X. T. Zhang and Z. G. Zhang, *J. Power Sources*, 2017, **364**, 234.
- 28 W. S. Hummers Jr. and R. E. Offema, *J. Am. Chem. Soc.*, 1958, **80**, 1339.
- 29 P. C. Mahakul, K. Sa, B. Das, B. Subramaniam, S. Saha, B. Moharana, J. Raiguru, S. Dash, J. Mukherjee and P. Mahanandia, *J. Mater. Sci.*, 2017, **52**, 5696.
- 30 X. T. Zhang, D. W. Chang, J. R. Liu and Y. J. Luo, *J. Mater. Chem.*, 2010, **20**, 5080.
- 31 S. Sakamoto, M. Okumura, Z. G. Zhao and Y. Furukawa, *Chem. Phys. Lett.*, 2005, **412**, 395.
- 32 Z. Fan, P. C. Li, D. H. Du and J. Y. Ouyang, *Adv. Energy Mater.*, 2017, **7**, 1602116.
- 33 P. T. Yan, R. J. Zhang, J. Jia, C. Wu, A. G. Zhou, J. Xu and X. S. Zhang, *J. Power Sources*, 2015, **284**, 38.
- 34 Q. Xue, H. J. Zhang, M. S. Zhu, Z. X. Pei, H. F. Li, Z. F. Wang, Y. Huang, Y. Huang, Q. H. Deng, J. Zhou, S. Y. Du, Q. Huang and C. Y. Zhi, *Adv. Mater.*, 2017, **29**, 1604847.
- 35 D. Yoo, J. Kim, S. H. Lee, W. Cho, H. H. Choi, F. S. Kim and J. H. Kim, *J. Mater. Chem. A*, 2015, **3**, 6526.
- 36 C. Chen, M. Boota, X. Q. Xie, M. Q. Zhao, B. Anasori, C. E. Ren, L. Miao, J. J. Jiang and Y. Gogotsi, *J. Mater. Chem. A*, 2017, **5**, 5260.
- 37 M. R. Lukatskaya, S. M. Bak, X. Q. Yu, X. Q. Yang, M. W. Barsoum and Y. Gogotsi, *Adv. Energy Mater.*, 2015, **5**, 1500589.
- 38 M. R. Lukatskaya, S. Kota, Z. F. Lin, M. Q. Zhao, N. Shpigel, M. D. Levi, J. Halim, P. L. Taberna, M. W. Barsoum, P. Simon and Y. Gogotsi, *Nat. Energy*, 2017, **2**, 17105.
- 39 Y. N. Li, G. Y. Ren, Z. Q. Zhang, C. Teng, Y. Z. Wu, X. Y. Lu, Y. Zhu and L. Jiang, *J. Mater. Chem. A*, 2016, **4**, 17324.
- 40 J. Wang, J. L. Polleux, J. Lim and B. Dunn, *J. Phys. Chem. C*, 2007, **111**, 14925.
- 41 J. L. Liu, J. Wang, C. H. Xu, H. Jiang, C. Z. Li, L. L. Zhang, J. Y. Lin and Z. X. Shen, *Adv. Sci.*, 2018, **5**, 1700322.
- 42 H. Y. Li, Y. Hou, F. X. Wang, M. R. Lohe, X. D. Zhuang, L. Niu and X. L. Feng, *Adv. Energy Mater.*, 2016, **28**, 1601847.
- 43 Y. P. Tian, C. H. Yang, W. X. Que, X. B. Liu, X. T. Yin and L. B. Kong, *J. Power Sources*, 2017, **359**, 332.
- 44 C. Couly, M. Alhabeab, K. L. Van Aken, N. Kurra, L. Gomes, A. M. Navarro-Suárez, B. Anasori, H. N. Alshareef and Y. Gogotsi, *Adv. Electron. Mater.*, 2018, **4**, 1700339.
- 45 Y. Y. Peng, B. Akuzum, N. Kurra, M. Q. Zhao, M. Alhabeab, B. Anasori, E. C. Kumbur, H. N. Alshareef, M. D. Ger and Y. Gogotsi, *Energy Environ. Sci.*, 2016, **9**, 2847.
- 46 H. B. Hu and T. Hua, *J. Mater. Chem. A*, 2017, **5**, 19639.
- 47 Z. M. Fan, Y. S. Wang, Z. M. Xie, X. Q. Xu, Y. Yuan, Z. J. Cheng and Y. Y. Liu, *Nanoscale*, 2018, **10**, 9642.
- 48 P. Li, W. H. Shi, W. X. Liu, Y. F. Chen, X. L. Xu, S. F. Ye, R. L. Yin, L. Zhang, L. X. Xu and X. H. Cao, *Nanotechnology*, 2018, **29**, 445401.
- 49 M. S. Zhu, Y. Huang, Q. H. Deng, J. Zhou, Z. X. Pei, Q. Xue, Y. Huang, Z. F. Wang, H. F. Li, Q. Huang and C. Y. Zhi, *Adv. Energy Mater.*, 2016, **6**, 1600969.
- 50 Z. S. Wu, Y. J. Zheng, S. H. Zheng, S. Wang, C. L. Sun, K. Parvez, T. Ikeda, X. H. Bao, K. Müllen and X. L. Feng, *Adv. Mater.*, 2017, **29**, 1602960.
- 51 K. Q. Qin, J. L. Kang, J. J. Li, E. Z. Liu, C. S. Shi, Z. J. Zhang, X. X. Zhang and N. Q. Zhao, *Nano Energy*, 2016, **24**, 158.
- 52 K. Q. Qin, E. Z. Liu, J. J. Li, J. L. Kang, C. S. Shi, C. N. He, F. He and N. Q. Zhao, *Adv. Energy Mater.*, 2016, **6**, 1600755.
- 53 Z. Y. Wang, S. Qin, S. Y. Seyedin, J. Z. Zhang, J. T. Wang, A. Levitt, N. Li, C. Haines, R. O. Robles, W. W. Lei, Y. Gogotsi, R. H. Baughman and J. M. Razal, *Small*, 2018, **14**, 1802225.